PAPER

Check for updates

A modern look at a medieval bilayer metal leaf: nanotomography of Zwischgold†

Qing Wu, [iD] [a,b] Karolina Soppa, [iD] [c] Elisabeth Müller, [iD] [d] Julian Müller,[e]
Michal Odstrcil,[d,f] Esther Hsiao Rho Tsai, [iD] [d,g] Andreas Späth, [iD] [h,i] Mirko Holler,[d]
Manuel Guizar-Sicairos,[d] Benjamin Butz,[e] Rainer H. Fink [iD] [h] and
Benjamin Watts [iD] *[d]

Many European sculptures and altarpieces from the Middle Ages were decorated with Zwischgold, a bilayer metal leaf with an ultra-thin gold face backed by silver. Zwischgold corrodes quickly when exposed to air, causing the surface of the artefact to darken and lose gloss. The conservation of such Zwischgold applied artefacts has been an obstinate problem. We have acquired quantitative, 3D nanoscale images of Zwischgold samples from 15th century artefacts and modern materials using ptychographic X-ray computed tomography (PXCT), a recently developed coherent diffractive imaging technique, to investigate the leaf structure and chemical state of Zwischgold. The measurements clearly demonstrate decreasing density (increasing porosity) of the leaf materials and their corrosion products, as well as delamination of the leaves from their substrate. Each of these effects speak to typically observed issues in the conservation of such Zwischgold applied artefacts. Further, a rare variant of Zwischgold that contains extremely thin multiple gold layers and an overlapping phenomenon of Zwischgold with other metal leaves are observed through PXCT. As supportive data, scanning electron microscopy (SEM) and scanning transmission electron microscopy (STEM) coupled with energy dispersive X-ray analysis (EDX) were performed on the medieval samples.

1 Introduction and background

Throughout the history of human civilization, lustrous gold has been a favoured material for displaying wealth, prestige and power. In the medieval material hierarchy, gold possesses the ultimate position, reflecting the splendour of God and representing the brilliance of divine wisdom, or simply the Holy Scripture.[1] The technical innovation of gilding, where thin leaves of gold are used to cover a surface, greatly reduced the cost of producing large "golden" artworks and significantly expanded the decorative use of gold.

A further innovation appeared in medieval Europe, whereby the gold leaf was backed by a relatively thicker, cheaper metal (usually silver) so that the expensive gold layer could be made thinner than contemporary gold leaf and hence reduced the gilding costs by at least half.[2,3] This new laminated metal leaf has been known by many names in different languages, *e.g. part-gold* in English,[4] *or parti* in French,[5,6] and *oro di metá* in Itatian,[7] but is now commonly referred to by the German word *Zwischgold*.[8–11] The production of Zwischgold is recorded to involve adhering a thin gold layer over a thicker silver base with a so-called "cold welding" technique.[8,9] The materials for producing Zwischgold were supposed to be fine gold and fine silver[12] and it is assumed that the gold was sourced from high quality gold coins, *e.g. florins* and *ducats*, in the same manner as contemporary gold leaf.[13] The silver component makes Zwischgold susceptible to corrosion and its surface tends to darken and lose its gloss when exposed to air. This occurs because Ag atoms readily diffuse through the grain boundaries

[a]University of Zurich (UZH), Rämistrasse 73, 8006 Zurich, Switzerland

[b]TH Köln – University of Applied Sciences, Ubierring 40, 50678 Köln, Germany. E-mail: qingaling@gmail.com

[c]Bern University of Applied Sciences (BUAS), Fellerstrasse 11, 3027 Bern, Switzerland. E-mail: karolina.soppa@hkb.bfh.ch

[d]Paul Scherrer Institute (PSI), Forschungsstrasse 111, 5232 Villigen-PSI, Switzerland. E-mail: elisabeth.mueller@psi.ch, michal.odstrcil@psi.ch, mirko.holler@psi.ch, manuel.guizar-sicairos@psi.ch, benjamin.watts@psi.ch

[e]Micro- and Nanoanalytics Group, Universität Siegen, Paul-Bonatz-Strasse 9-11, 57076 Siegen, Germany. E-mail: julian.mueller@uni-siegen.de, benjamin.butz@uni-siegen.de

[f]Carl Zeiss SMT, Carl-Zeiss-Straße 22, 73447 Oberkochen, Germany

[g]Brookhaven National Laboratory, Upton, New York 11973, U.S.A. E-mail: etsai@bnl.gov

[h]Friedrich-Alexander-Universität Erlangen-Nürnberg (FAU), Egerlandstraße 3, 91058 Erlangen, Germany. E-mail: andreas.spaeth@fau.de, rainer.fink@fau.de

[i]Institut für Nanotechnologie und korrelative Mikroskopie (INAM), Äußere Nürnberger Strasse 62, 91301 Forchheim, Germany

†Electronic supplementary information (ESI) available. See DOI: https://doi.org/10.1039/d2nr03367d

of the gold layer to reach the upper surface and then react with S and Cl in the presence of moisture.[14,15] In regions where the local guilds did not prohibit the use of Zwischgold, the application of a protective varnish was usually a requirement.[4,16] Since uncorroded Zwischgold applications are difficult to distinguish from gold leaf, it is probable that many Zwischgold examples remain unrecognised. However, many of the known late medieval Zwischgold-applied artefacts present a matte black surface, likely due to the degradation of the organic varnish materials over the centuries and subsequent silver corrosion.

The application of Zwischgold in artworks began on paintings of the early 13th century[4] and became popular in German sculptures from the 14th century.[17] Since it presents a real gold surface while requiring much less gold than normal gold leaf, it is typically thought that it was mainly used at the time as an economical alternative to gold leaf.[4,8,18–20] This theory is supported by many examples of Zwischgold being applied to less prominent areas, such as the rear or within concave clothing folds of altar sculptures,[21–23] especially with its corroded, darkened appearance that can be easily distinguished from the surrounding gold leaf surface. However, modern scientific analysis reveals that Zwischgold has also been applied prominently, for example, in the Leiggern Altar from the Swiss National Museum (SNM) presented in Fig. 1a, the entire outer gown of the central Mary figure, the clothes of three floating angels, hair/beard of some wing figures, and the top frames of the shrine were applied with Zwischgold.[24–26] In such a case, economic considerations seem less convincing. The complexity of Zwischgold's structure and the reasons for its application make it an interesting topic for research in art history and art technology.

The techniques for applying Zwischgold onto its substrate were similar to those for gold leaf, among which the bole gilding and oil gilding techniques were most commonly used.[4,27] Bole gilded Zwischgold leaves were directly applied on the bole substrate with an aqueous solution and, once dry, burnished with agate or animal horn to smoothen the surface to a high gloss. Fig. 1b presents typical examples of Zwischgold applied to limited areas of two late medieval gilded sculptures, showing dark patches where silver has diffused through to the surface and strongly tarnished.[15] One of the very few exceptions is the central figure Mary of the Leiggern Altar, which still appears golden in colour (if somewhat dark) and retains gloss. As such, Mary provides a good opportunity to obtain a sample that is well known to contain medieval Zwischgold that has not been heavily corroded.

Ptychographic X-ray computed tomography (PXCT) is a 3D imaging technique that, instead of using image-forming optics, uses iterative mathematical routines to analyse the X-ray scattering patterns of a sample as a function of rotation and translation to reconstruct a full 3D image of the refractive index variations within the sample.[28–31] The resolution of ptychography is not given by the scanning step nor by the beam size, as with scanning probe microscopy, but rather by the widest-angle scattering observed that correspond to the shortest-length features, or sample variations.[32,33] PXCT is thus among the X-ray techniques with the highest resolving power.[34–37] PXCT provides a quantitative measure of the complex-valued refractive index (both absorption β and refraction δ) distribution in a specimen. Measurements performed with hard X-rays tend to show higher contrast in δ due to the high penetration power (low absorption) of hard X-rays. While measurements using an X-ray energy close to an elemental resonance can be used to increase sensitivity to particular materials, utilising an X-ray energy far from such resonances will provide β and δ values that both correlate roughly proportional to the mass density of the sample materials. Hence, given some foreknowledge of the sample composition, the identity of a material

Fig. 1 (a) The central altar figure Mary (Inv. No. LM16701.2) in the Leiggern Altar (Inv. No. LM16701.1), 1420, Swiss National Museum (SNM); (b) sculptures St. Bishop (Inv. No. 1941.282) (left) and St. Nicolaus (Inv. No. 1941.281) (right), 15c, Historical Museum Basel (HMB), Switzerland. The sample-taking positions are indicated by green arrows.

can be inferred from the measured local δ values, together with variations in composition and/or porosity.[30]

Due to its ultra-thin leaf thickness (*e.g.*, 500–700 nm for modern Zwischgold[15] and significantly thinner for medieval Zwischgold[38]), a characterisation of Zwischgold requires both high resolving power and high sensitivity and is thus challenging for conventional techniques. Recent work by our collaboration group[15,26,38,39] has demonstrated the use of modern analytical techniques such as SEM-EDX to identify and characterise modern and historical Zwischgold including its leaf structures and layer/leaf thicknesses, as well as its complicated individual ageing phenomena. These typically involve the formation of silver compounds that can be distributed evenly or in aggregates in regions surrounding the gold layer, and consumption of the silver base which leads to delamination of the metal leaf from the substrate. However, the 2D cross-sectioning techniques provide only a limited view of the whole, complex scenarios that are observed in historical Zwischgold samples. Three dimensional imaging will certainly provide more informative views of real objects than 2D cross-sections, although the degree to which this is useful has not yet been fully explored since nanoscale 3D imaging is relatively new and still not easily accessible. Further, sectioning historical Zwischgold samples is challenging due to the fragile nature of the specimens; the substrates can be porous and brittle and the leaf poorly adhered, while the corrosion products and organic overlayers can be chemically and mechanically unstable. Hence there is a strong possibility for any sectioning technique to alter the sample materials and structures at the cutting face. Therefore, we have applied PXCT to both modern and historical Zwischgold samples, so that the structures and chemical states of the Zwischgold and surrounding materials can be observed in quantitative, 3D nanoscale images. The PXCT will provide valuable observations of interior regions of Zwischgold samples away from the cutting face and thus test the validity of previous Zwischgold observations by conventional techniques. The quantitative nature of the PXCT data will also provide opportunities for novel observations.

2 Samples

In order to demonstrate the analysis of Zwischgold by PXCT and provide a basis for comparison, a set of three modern and four medieval samples were measured together with a pure gold reference (impurities <100 ppm; *Heraeus*, Germany).

Two freestanding Zwischgold leaves (*Recent* and *10-year*) were included in the modern samples: one recently manufactured (using 23.2 carat gold; *Noris Blattgold*, Germany), and another manufactured approximately 10 years ago (manufacturer unknown). Both of these had been stored in their original packaging in a cool, dry cupboard. A third modern sample (*35-year*) was taken from an unvarnished and strongly corroded area of a 35-year old Zwischgold demonstration object at the Bern University of the Arts. The *Recent* and *35-year* old Zwischgold samples have been characterised in a previous

publication.[15] Although the original manufactured purity of the Au layer in the *10-year* and *35-year* old Zwischgold samples are not precisely known, it is very likely that the tradition of using high-purity gold and silver was followed and they are similar to that of the *Recent* Zwischgold sample. Elemental analysis by Energy Dispersive X-ray (EDX) and X-ray Fluorescence (XRF) analysis (see Fig. S1 and S2 in the ESI†) did not reveal significant amounts of other metals, especially copper, which would be the most likely indicator of lower-quality gold and silver.[40,41]

The Leiggern Altar (Fig. 1a) is thought to have been produced in the region of Ulm, Southern Germany in 1420.[42] At the time of its purchase by the Swiss National Museum in 1925, it was displayed in the Leiggern mountain chapel in Ausserberg (Valais, Switzerland) and from 2019 has been on permanent exhibition in Zurich. The altar figure *Mary* (size: *H* 112.5 × *B* 44.5 × *D* 25 cm) stands at the centre of the Leiggern Altar. Previous X-ray fluorescence measurements indicated extensive use of gold, silver and Zwischgold leaves.[25] The Zwischgold-applied outer gown of Mary appears well preserved, but is known to have been partly applied with gold leaf during restoration treatments in the past; hence the sample *Mary* was taken from an area, indicated in Fig. 1a by a green arrow, where we expect that only original Zwischgold is present.[25] A 1974 investigation[24] on the altar figure *Mary* described an organic varnish layer applied to the top surface of the object, which has been confirmed by our SEM-EDX measurements showing significant amounts of C and O in the top layer of a sample cross-section (see Fig. S5 in the ESI†). SEM measurements further provide evidence for a presence of Fe-containing particles in the substrate and Zn-containing particles in the varnish (see Fig. S5†). The former indicates the use of bole gilding techniques.[8,43,44] The source of Zn-containing particles is uncertain; possibly some Zn compounds were used as siccative during the drying process of an oil-based varnish.[45,46]

Two 15-century polychrome wooden sculptures *St. Bishop* and *St. Nicolaus* were acquired by the Historical Museum Basel (HMB, Switzerland) *via* a private donation from Sedrun (Grisons, Switzerland) in 1941.[47] Further details of their origin and history are not available. Fig. 1b shows that these sculptures contain dark, matte patches on their golden gowns, which is indicative of corroded Zwischgold. Two samples (*Bishop* and *Nicolaus*) were taken from the centre of a darkened patch on each object and an extra sample (*Nicolaus Border*) was taken from the border area of a darkened patch next to the neighbouring gold surface. These three samples exhibit much stronger corrosion phenomenon than the *Mary* sample, which can be easily discerned by eye and has been further confirmed through the SEM-EDX measurements (Fig. S12, S13 and S14 in the ESI†).
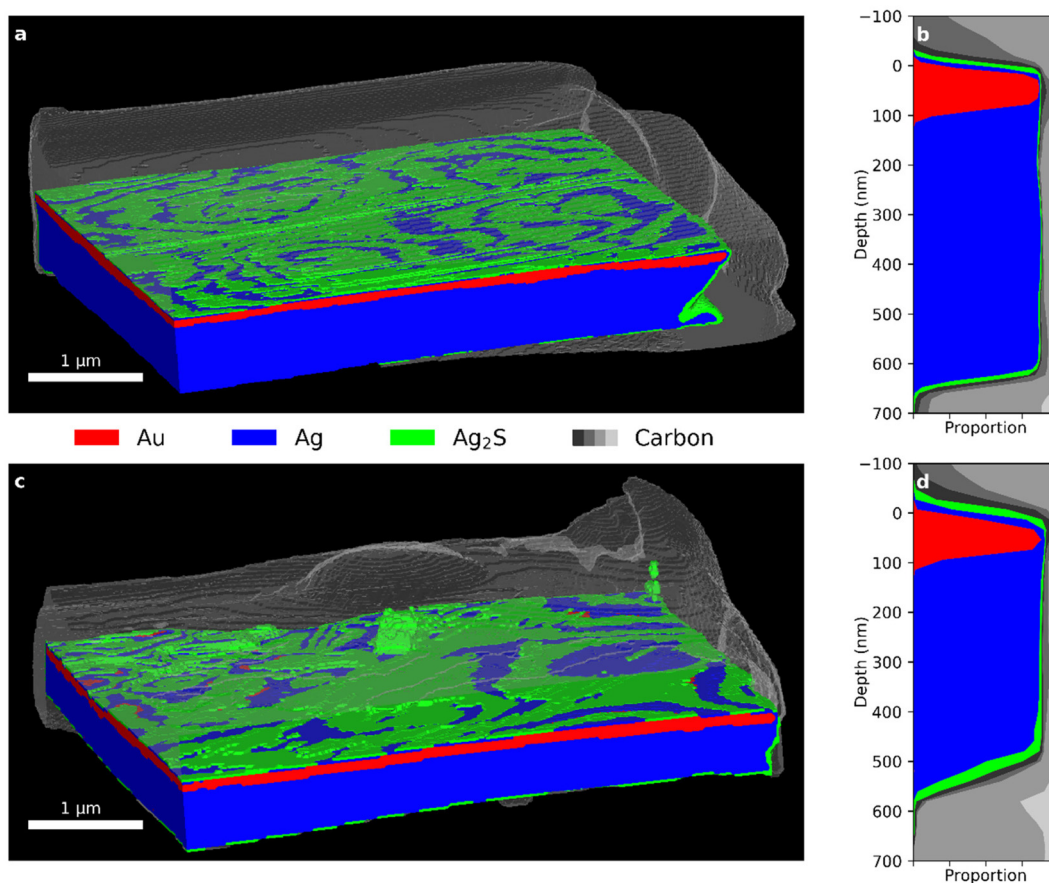
3 Results and discussion

3.1 Modern Zwischgold

Fig. 2 shows views of the PXCT 3D images and stack plots of the integrated depth profiles for the (a and b) *Recent* and (c

Fig. 2 (a) Segmented PXCT 3D view and (b) depth profile of the *Recent* sample. (c) Segmented PXCT 3D view and (d) stack plot of the depth profile of the *10-year* sample. (See Fig. 3 for further segmentation details.).

and d) *10-year* Zwischgold leaf samples. Two front-facing edges of the samples have been digitally removed to show an internal cross-section. An expected structure of a thin gold layer atop a thicker Ag layer has been revealed, with a thin outer covering of silver corrosion products that appears relatively thicker in the older, *10-year* sample. Some carbon-based material that was deposited during FIB preparation surrounds the samples. The stack plots in Fig. 2b and d show the relative proportion of each segment (by the amount of colour along a horizontal line) as a function of their depth below the leaf surface (analysis details are provided in the ESI†). Both samples show the same general structure with a red band above a thicker blue band representing the Au segment layer above the Ag segment layer of the Zwischgold leaf. The grey bands running down the right hand side (also at the top and bottom) represent the FIB-deposited carbon material around the samples that was used to hold them in place. We can estimate the thickness of the layers *via* a full width at half maximum (FWHM) measure by examining the change in depth of the segment at the percentage composition value that is half of the segments maximum (*i.e.* by looking at the profile sideways). In this way, we find thicknesses of the *Recent* and *10-year* gold layers to be 81.8 and 74.5 nm respectively, while the corresponding FWHM of the combined Au and Ag (red and blue) segments give full leaf

thicknesses of 629 and 505.3 nm respectively. These thicknesses compare well with recently published SEM measurements of a leaf from the same pack as *Recent*, with gold layer and full leaf thickness of 93 ± 19 and 573 ± 71 nm.[38]

Further detail can be seen in Fig. 3, which presents δ histograms from PXCT measurements of the gold reference together with the *Recent*, *10-year* and *35-year* modern Zwischgold leaves. The main materials of interest, namely the metallic Au and Ag, are expected to be observable in peaks located at δ-values of approximately 40×10^{-6} and 25×10^{-6}, while the main corrosion products (*i.e.*, Ag_2S and AgCl) are expected to be significantly porous and so should produce peaks at δ-values lower than the 17.6×10^{-6} and 13.6×10^{-6} calculated from their respective bulk densities. Previous EDX measurements[15] and complementary XPS measurements (see Fig. S16†) confirmed the dominance of Ag_2S in the *35-year* sample and therefore the peak centred at 15×10^{-6} is attributed to Ag_2S. Since this Ag_2S peak position has a δ-value approximately 15% lower than expected for the bulk material, we conclude that the observed material has a 15% decrease in density due to porosity below the resolution of this measurement. The weak peaks observed near 10.5×10^{-6} in the *10-year* and *35-year* histograms would fit to AgCl with a similar porosity to that of the observed Ag_2S. The peaks at δ-values of $7.0 \times$
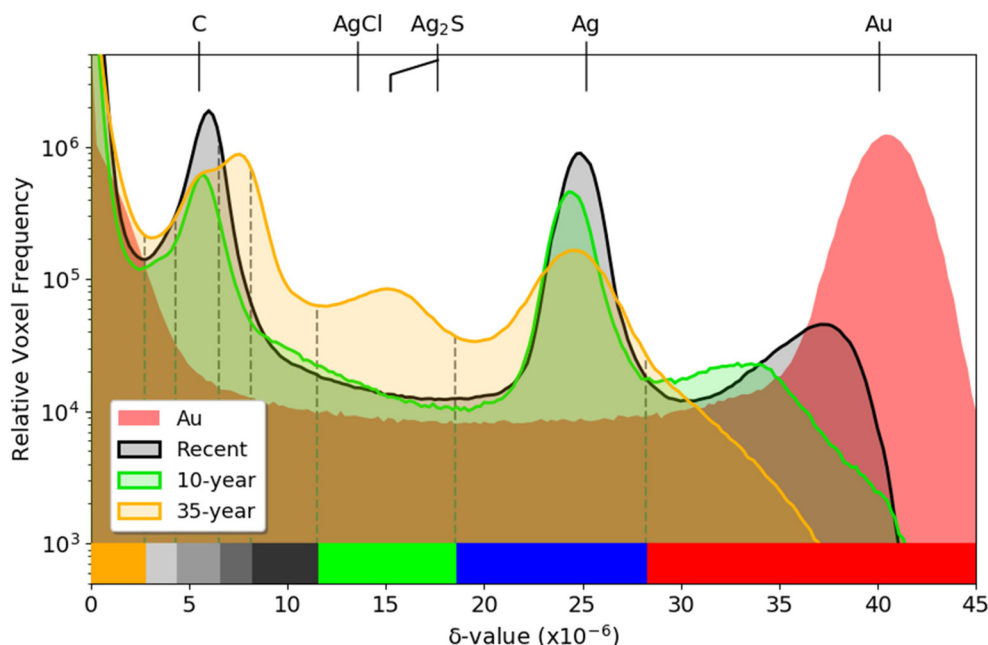
Fig. 3 Comparison between the PXCT δ-value histograms of the *Recent*, *10-year*, and *35-year* samples and a pure gold reference. The histograms have been scaled to match the average number of total voxels with a δ-value above 3×10^{-6} in order to normalise against different sample sizes. The colour bar along the lower edge indicates the segmentation for the PXCT tomogram presentations shown in other figures.

Table 1 Imaging parameters of each PXCT tomogram, detailing the field of view (FOV; horizontal and vertical), step size of the Fermat spiral scan, the number of projections and total data collection time, as well as the reconstruction pixel size and the 3-dimensional resolution estimate by Fourier shell correlation (FSC) using the 1/2 bit threshold

Sample	FOV ($H \times V$ µm)	Step size (µm)	Projections	Time (h)	Pixel size (nm)	3D FSC (1/2 bit; nm)
Recent	13 × 6	0.6	820	15	12.12	18
10-year	13 × 6	0.7	870	18	20.27	24
35-year	15 × 6	0.6	700	13.2	15.3	35
Mary	10 × 5	0.6	480	6	15.3	30
Bishop	12 × 6	0.6	400	6.8	15.3	39
Nicolaus	10 × 5	0.6	800	9.8	15.3	19
Nicolaus Border	12 × 10	0.6	548	14.3	15.3	36
Au reference	6 × 6	0.6	160	1.7	15.3	—

10^{-6} and 7.9×10^{-6} in the *35-year* histogram are attributed to materials in the substrate, while the peak near 5.7×10^{-6} is due to the carbon layer deposited on the sample surface to protect it from Ga^+ ion implantation during sample preparation by focused ion beam (FIB) milling. Air surrounding the measured samples produces a strong peak at a δ-value of zero. Table S1 in the ESI† lists additional candidate component materials and their calculated X-ray refractive indices.

A striking trend in the histograms in Fig. 3 is that the rightmost (highest δ) peak, which corresponds to the highest density material observed in the samples, only matches the δ-value calculated for bulk gold in the case of the pure gold reference sample. The *Recent* and *10-year* leaf samples show their highest-δ peaks at 36.5×10^{-6} and 32×10^{-6}, respectively, while the *35-year* sample shows only a monotonic decline as the δ-value increases above the Ag peak position. While this is partly due to

the smaller amount of gold present in the older samples, blurring and volume-mixing artefacts of the imaging technique tend to reduce the apparent δ-values of the Zwischgold gold layers, especially those that have a similar thickness to the imaging resolution (see Table 1) and are surrounded by much lower-δ materials. The alternative explanation that the gold is significantly decreasing in density or purity with time is contrary to the well-known chemical inertness and low diffusivity of gold lattices.[48–51] Indeed, STEM-EDX measurements of the medieval *Mary* sample, discussed in detail in the following section, demonstrate that the gold layer of Zwischgold retains its purity and density over long time scales.

More subtle movement of the Ag peak is also observed in Fig. 3, shifting from 24.8×10^{-6} in the *Recent* sample, to 24.4×10^{-6} in the *10-year* sample and to 24.5×10^{-6} in the *35-year* sample, indicating a 1.6%, 3.2% and 2.8% respective decrease

from the δ-value of 25.2×10^{-6} calculated for bulk Ag. This decrease is interpreted as an increase in porosity in the Ag, due to the *Kirkendall* effect.[52] The Ag peak of the *35-year* histogram is also much lower and broader than the *Recent* and *10-year* ones; since the broadening is roughly symmetric and porosity can only make a material less dense (*i.e.* move a voxel to the left in the histogram), we expect that this is also an effect of the imaging resolution.

Fig. 4 displays segmented 3D visualisations from PXCT measurements of the *35-year* Zwischgold sample, with exposed cross-sections and stepwise addition of materials in order to highlight details in each layer. These tomograms have been segmented according to the δ-ranges indicated by the colour bar along the bottom of Fig. 3. The view in Fig. 4a shows only the red "Au" segment, while the view in Fig. 4b adds the blue "Ag" segment and shows translucent surfaces of the internal voids (which are shown in orange in Fig. 4d). Fig. 4c displays the Au and Ag segments together with the green "silver sulphide" segment (centred on the 15% porous Ag_2S peak). Finally, Fig. 4d displays all material segments, including the greyscale segments attributed to the bole, varnish and FIB-protection materials. Internal voids are shown as an orange segment. While the *Recent* and *10-year* leaf samples (Fig. 2) display consistent and even layers of gold material over silver, the gold layer of the *35-year* sample (Fig. 4a) is much thinner and shows strong thickness variations and no longer appears to form a continuous layer (or perhaps gets thinner than the imaging resolution). Fig. 4e shows an area-integrated depth profile (aligned to the upper surface of the gold layer) of the single-layered section of the *35-year* sample that demonstrates the proportions of the material segments as a function of depth below the leaf surface. The FWHM thickness of the Au

segment gives a gold layer thickness of 47.9 nm, which is similar to the 3D Fourier shell correlation estimate of the PXCT image resolution of 35 nm (see Table 1) and suggests that the observed FWHM gold layer thickness is not reliable. The observed gaps in the Au segment in Fig. 4a could also be a consequence of insufficient imaging resolution rather than actual gaps in the gold layer of the Zwischgold leaf. Fig. 4e shows a depth profile of a single-layer section of the *35-year* sample; here we see a second red Au segment peak near 400 nm depth that indicates a thin layer of increased δ-value at the lower edge of the silver layer (also visible on the left edge of the leaf in Fig. 4b). One could speculate that this thin layer is gold material transferred to the bottom of the leaf by contact with gold-contaminated manufacturing equipment.

Adding the Ag segment in Fig. 4b shows that a significant amount of the silver backing layer of the Zwischgold leaf remains intact. A flattened, S-shaped crease can also be observed in the metal leaf towards the right-hand edge of the tomogram. Wrinkles are commonly formed when a gilding leaf is initially laid onto the substrate and the surface is typically then burnished (rubbed with a tool) in order to flatten and compress these wrinkles to obtain a flatter, more shiny surface. The crease observed in Fig. 4 is approximately 2 microns wide at the front edge of the sample and gradually narrows to a point at the sample's rear. Burnishing of the surface also appears to have dragged some metal across the trough next to the creased leaf, demonstrating that burnishing a metal leaf surface can do more than simply compressing ridges. This burnished surface layer is also visible in distribution of Au and Ag in the depth profile between -250 nm and the surface of the main gold layer.

Adding further components to the tomogram in Fig. 4c and d, we observe a layer of silver sulphide (green) over the metal
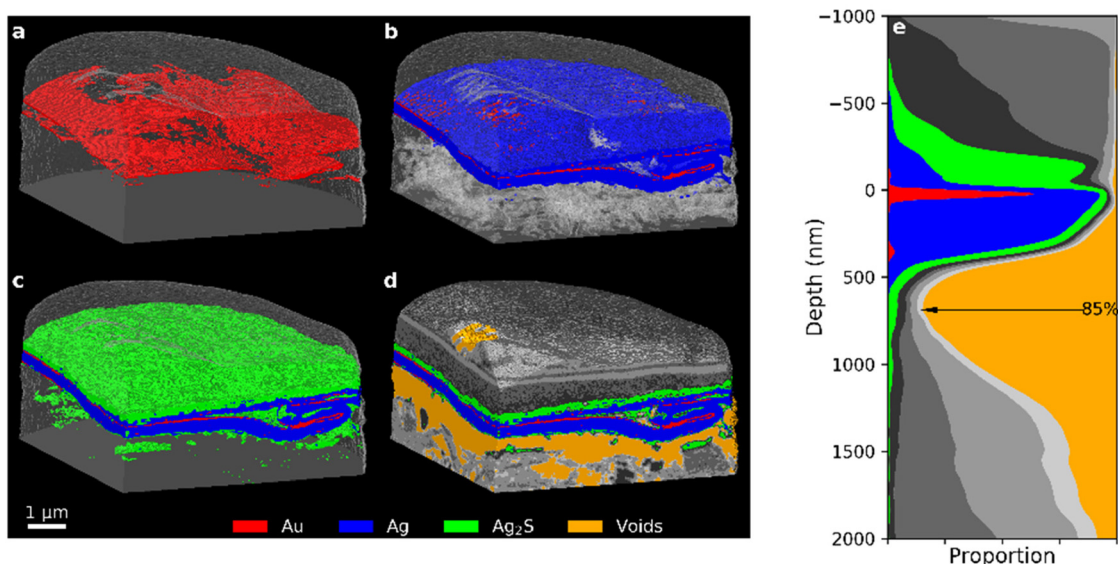
Fig. 4 PXCT 3D images of the *35-year* old Zwischgold sample showing the addition of (a) Au, (b) Ag (with transparent voids), (c) "silver corrosion products", and (d) other segments (see Fig. 3 for segmentation details). (e) Stack plot of the depth profile of the single-layered section of the sample, aligned to the main layer of the Au segment.

layers and a few clusters below. The dark grey clusters just below the metal leaf appear consistent with porous silver chloride in both δ-value and spatial arrangement. Previous measurements of corroded Zwischgold have shown that the silver sulphide layer becomes substoichiometric close to the metal interface.[15] The δ-values used to segment the PXCT data scale roughly linearly with material density and so it is not possible to distinguish between small changes in elemental composition and variations in material porosity. Examining the orange segment representing internal voids in Fig. 4d, we clearly observe a significant gap that has opened between the metal leaf and the bole substrate. The extent of the gap can also be clearly seen in the depth profile, where the void occupies approximately 85% of the cross-sectional area just below the metal leaf. Previous observations of such gaps in neighbouring sections of the same sample[15] showed a much smaller separation that was consistent with consumption of the silver layer, however, the gap observed here clearly involves mechanical movement of the metal leaf away from the substrate. We hypothesise that the gap observed here may have been caused, or increased, by differential expansion and contraction of the metal leaf and the substrate during temperature and humidity cycles over the lifetime of the object. While it is possible that heating of the sample during FIB preparation[53] is at least partly responsible for the separation of the metal leaf from its bole substrate, similar measurements on the medieval Zwischgold samples did not show the same pattern of voids in all cases and so indicate that the observation of leaf-substrate separation is likely not just an experimental artefact.

3.2 Medieval Zwischgold

PXCT 3D views of the *Mary* sample in Fig. 5, show structural similarities to the *35-year* old modern Zwischgold sample shown in Fig. 4, with a gold layer above a silver layer that is undercut by a concentration of voids. In the case of *Mary*, however, the gold layer is overall thicker, but very irregular with thickness variations textured at length scales of about 200 nm. Horizontal migration of Au away from grain boundaries is an expected consequence of Au–Ag grain-boundary diffusion, which suggests that this pattern is influenced by the pattern of grain boundaries in the initial gold layer,[14,54] however this would be an extremely large scale to observe grain boundary widening and it is not supported by complementary STEM measurements (Fig. 6) discussed below. This variation is reflected in the depth profile shown in Fig. 5e, where the gold segment forms a much broader and less intense peak than that observed for the modern samples. The silver layer in this specimen is also significantly thinner than that of the modern samples and so the total Zwischgold thickness is correspondingly lower. The FWHM thicknesses of the gold layer and full leaf are 126.5 and 251.7 nm, respectively. STEM (Fig. 6) and SEM (Fig. S5†) measurements of adjacent sample cross-sections also show large variations in the gold layer thickness, although with an average thickness below 100 nm. Previous SEM measurements of another adjacent sample[38] observed a thinner and more even gold layer thickness of only 56 ± 26 nm over 71 positions (and a similar full leaf thickness of 307 ± 68 nm). Kitagawa[54] showed that when
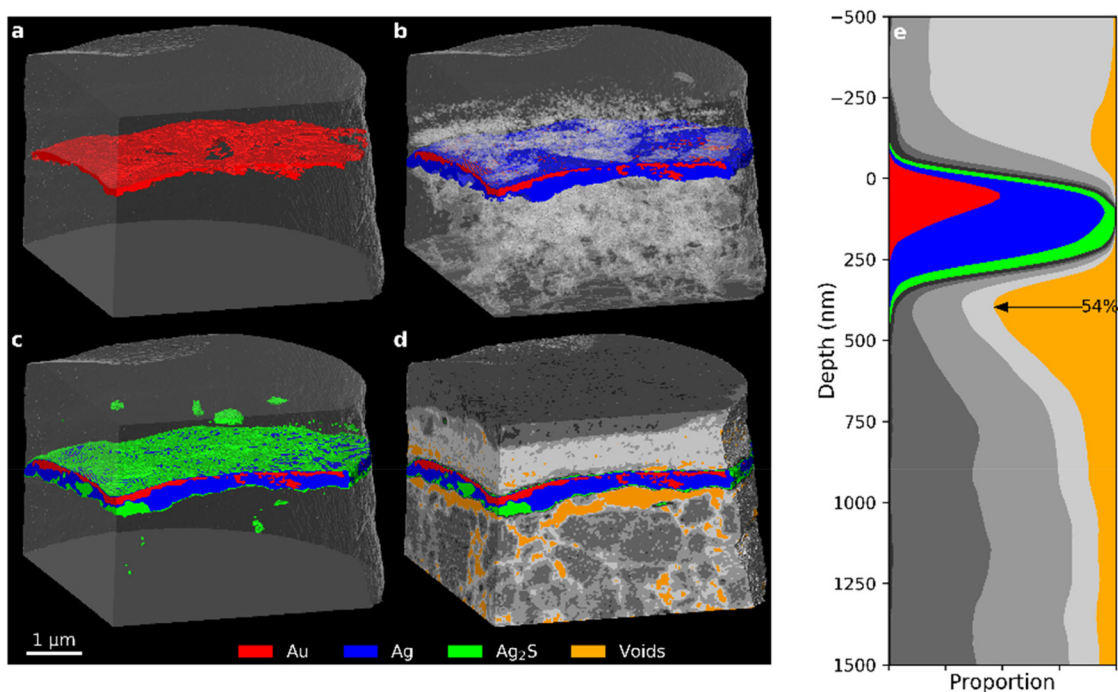
Fig. 5 PXCT 3D images of the *Mary* sample showing the addition of (a) Au, (b) Ag (with transparent voids), (c) "silver corrosion products", and (d) other segments (see Fig. 7 for segmentation details). (e) Stack plot of the depth profile of the sample, aligned to the main layer of the Au segment.
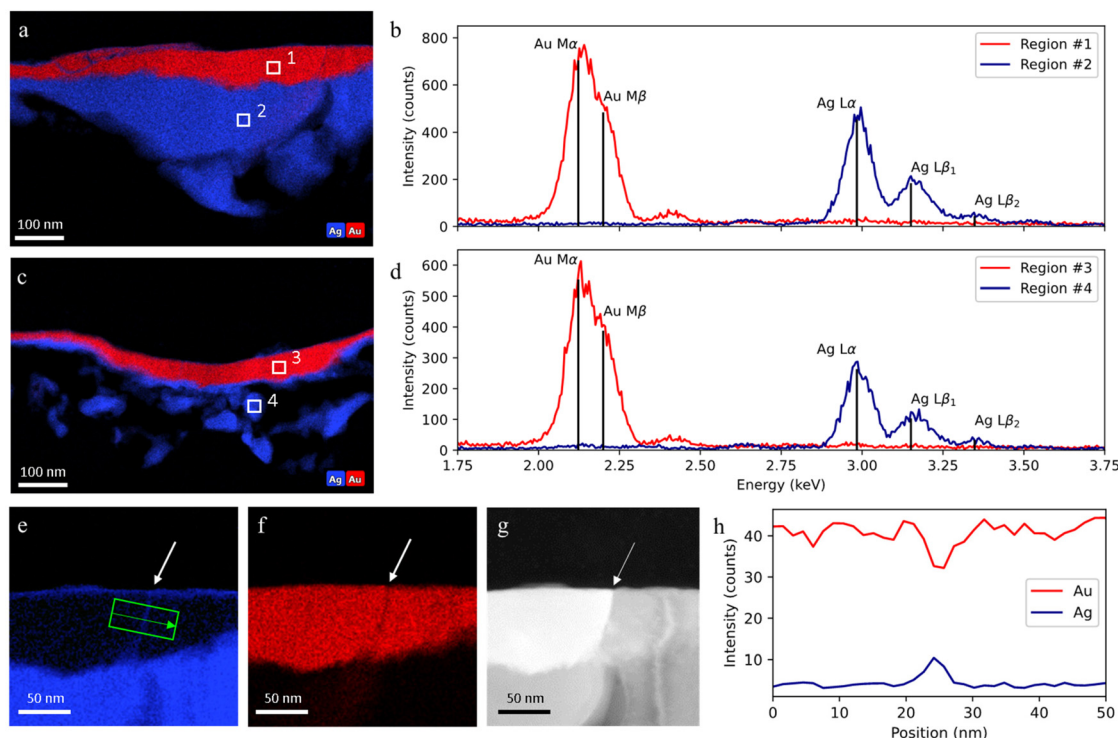
Fig. 6 STEM-EDX analysis of a sample taken in an adjacent region to the *Mary* sample: (a and b) EDX elemental maps for Au and Ag, and EDX spectra of area 1 and 2; (c and d) EDX elemental maps for Au and Ag, and EDX spectra of area 3 and 4; (e–g) EDX Au and Ag maps and high-angle annular dark-field (HAADF) image of a gold grain boundary filled with silver atoms; (h) EDX line profile across a gold layer grain boundary (along the green arrow). Sub-panels (e–h) reproduced from ref. 38.

hammered into leaf, gold and silver will retain relatively large grains that preferentially deform in specific ways that keep the metal leaf uniform during the hammering process. The strong variations in gold layer thickness observed in *Mary* suggest that the manufacture of the Zwischgold leaf involved uneven hammering.

Further evidence of the limits of the PXCT analysis is provided by an EDX analysis through STEM (operating with a resolution of a few nanometers) on a sample taken in an adjacent region of the *Mary* sample, shown in Fig. 6. Fig. 6a–f demonstrates that there is a clear separation between the gold and silver layers and that these layers have purities of more than 98 at% and 99 at% respectively. Such observations indicate that no significant lattice interdiffusion has occurred in this 600-year old Zwischgold sample. However, grain boundary diffusion is expected to occur rapidly and can be observed in Fig. 6e–h as a narrow line of Ag crossing the gold layer at the boundary between crystalline grains. The grain boundary is observed to be about 5 nm wide and so grain boundary broadening cannot be a significant contribution to the strong gold-thickness variations observed in the *Mary* sample.

The distribution of (green) silver sulphide in the *Mary* sample (Fig. 5c) shows two modes. The surfaces of the metal leaf are covered by a very thin layer of corrosion products, but there are also some bulk regions where the metallic silver layer of the leaf has been replaced by silver sulphide. The layers

adjacent to the Zwischgold leaf in the *Mary* sample also show interesting features in Fig. 5. The supporting substrate is much more structured than that of the *35-year* sample, showing higher δ-valued grains within a lower density matrix that contains a well-connected pore network with voids on the scale of 100–300 nm. Further, the depth profile in Fig. 5e demonstrates that these voids show a concentration at the underside of the metal leaf that reaches over 50% of the total leaf area, meaning that less than half of the leaf area remains attached to the bole substrate. The relatively low-δ and smooth varnish layer similarly shows pores and although they are also concentrated close to the leaf interface, they are much less connected and only sum up to 11.2% detachment of the leaf-varnish interface. These voids do not correlate with the consumption of the silver layer, and are more consistent with mechanical detachment *via* differential expansion-contraction as discussed above for the *35-year* PXCT.

Examining the histograms of the medieval Zwischgold samples in Fig. 7, we observe a similar set of peaks to that of the modern samples, but with much lower counts at the δ positions corresponding to Ag and Au and an additional peak located at a δ value of about 10×10^{-6}. While the *Nicolaus Border* shows a strong profile extending to very high δ values, the PXCT images in Fig. 8 reveal a completely different situation from the other samples where the main gold segment is below the silver segment and in some places separates into up
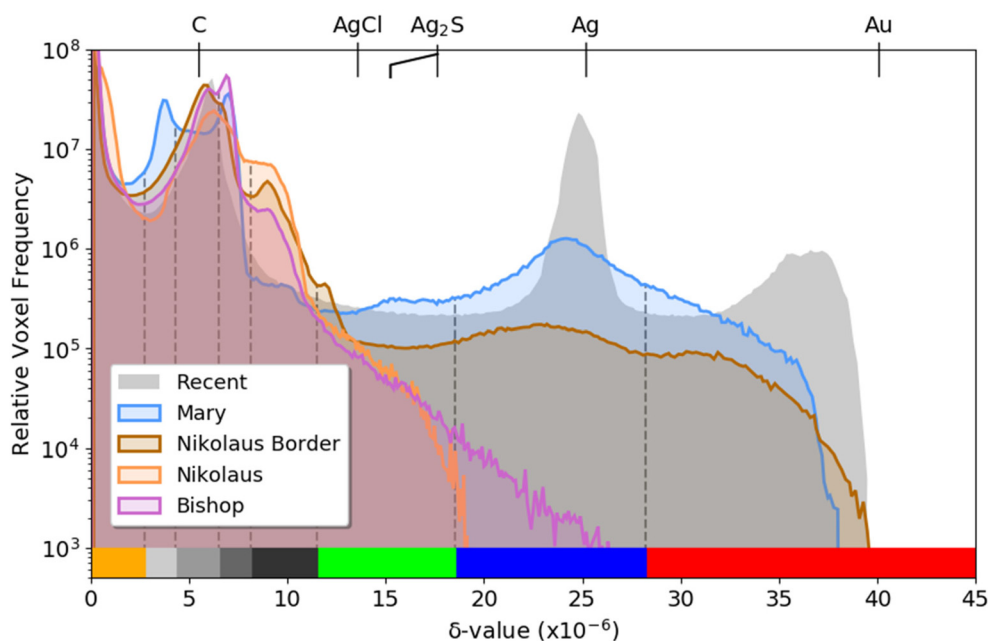
Fig. 7 Comparison between the delta value histograms of the samples *Nicolaus Border*, *Nicolaus*, *Bishop* and *Mary*, together with the *Recent* histogram for a comparison to modern Zwischgold. The data has been median-filtered in order to decrease peak widths and the histograms have been scaled to normalise against different sample sizes. The colour bar along the lower edge indicates the segmentation for the PXCT 3D model presentations shown in other figures.
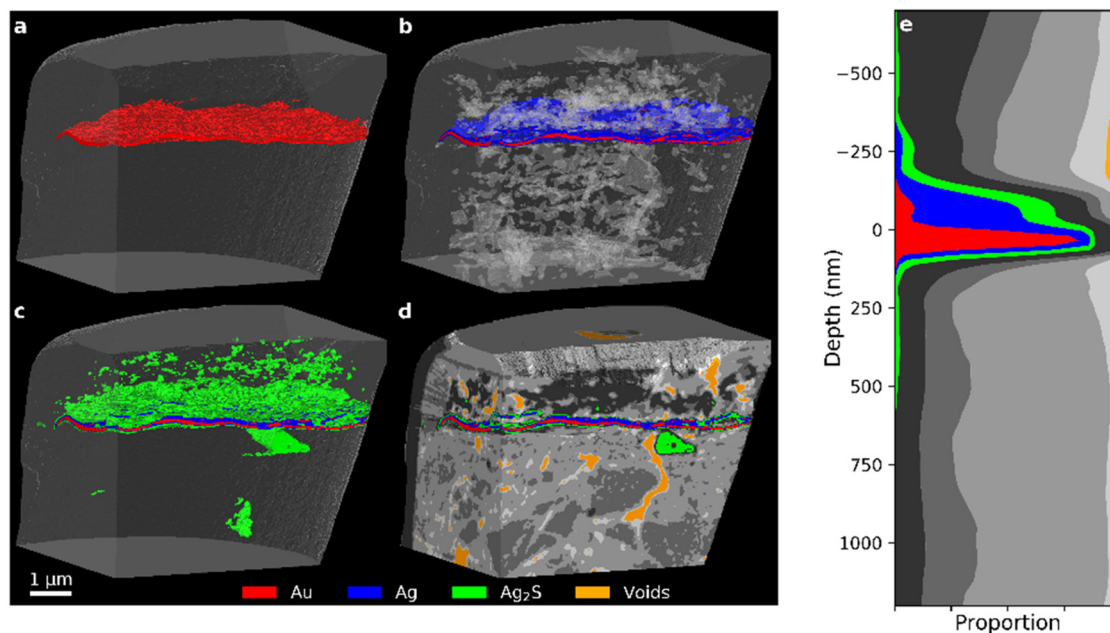

Fig. 8 (a–d) PXCT 3D images for different components (see Fig. 7 for segmentation details) inside the *Nicolaus Border* sample. (e) Stack plot of the depth profile of the sample, aligned to the main gold layer.

to 3 layers. A clearer view of these layers is provided in Fig. 9 with a slice through the PXCT tomogram (a and b) and an SEM image (c) of a separate cross-section region of the *Nicolaus Border* sample, revealing that there are in fact three gold layers; the lowest layer is about 106 ± 24 nm thick, while the middle and upper layers are about 41 ± 16 nm thick. The mismatch between PXCT and SEM data in Fig. 9 clearly demonstrates that the high δ of these thin gold layers has been blurred across adjacent PXCT voxels, which effectively shifts the high-δ counts of the corresponding histogram in Fig. 7 to
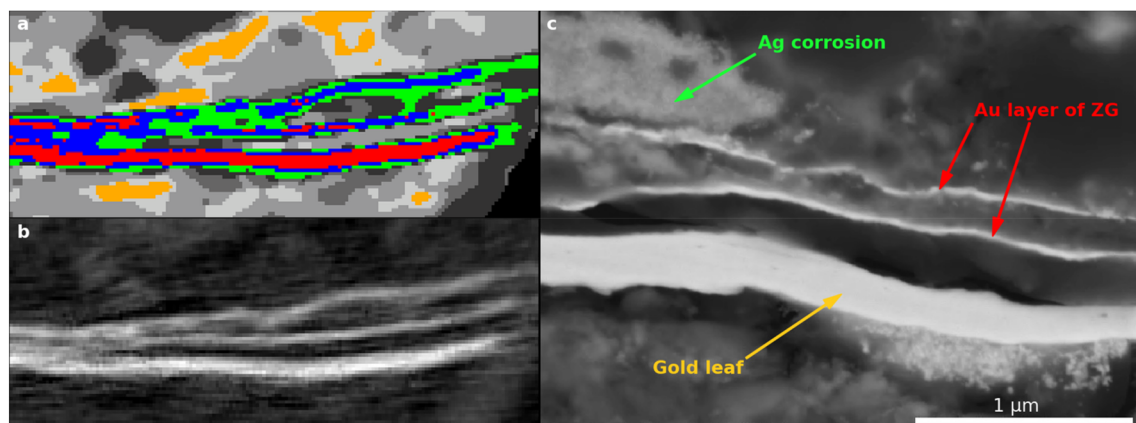
Fig. 9 (a) A segmented and (b) raw PXCT tomogram slice for *Nicolaus Border*; (c) SEM image of a microtomed cross-section of the "Nicolaus Border" sample labelled with observations from EDX analysis. Scale bar applies to all images.

lower δ, where they fall into another segmentation bracket. Complementary EDX analysis of the *Nicolaus Border* sample (Fig. S12 in the ESI†) further reveals that a mixture containing elements Ag, S, Ca, O and C deposits mainly above the top gold layer. Such observations indicate that a two-layered Zwischgold leaf overlaps a normal gold leaf, and the metallic silver in the Zwischgold leaf has largely transformed into silver corrosion products (*e.g.* Ag_2S), mixing with the varnish materials. This is consistent with the fact that the sample was taken from a border area between surfaces applied with Zwischgold and gold leaf. The presence of the gold leaf provides a significant number of gold voxels, contributing significantly to the highest δ segment of the histogram and exhibit-

ing a similar profile as the *Mary* sample. The *Mary* histogram does not show a distinct peak for silver sulphide, but rather shows a gradual transition between the Ag peak and the δ-position of the 15% porous Ag_2S peak observed for the *35-year* sample, indicating significant variation in the stoichiometry and porosity.

Although EDX analysis identifies silver sulphide as the main silver corrosion product in the *Nicolaus Border* sample, no peak is visible at 15×10^{-6} in the histogram presented in Fig. 7 as we have observed for 15% porous Ag_2S in *Mary* sample. We do, however, see a peak at 12.1×10^{-6} that is spatially associated with regions close to the silver segment in Fig. 7 and so probably consists of Ag_2S that is either twice as
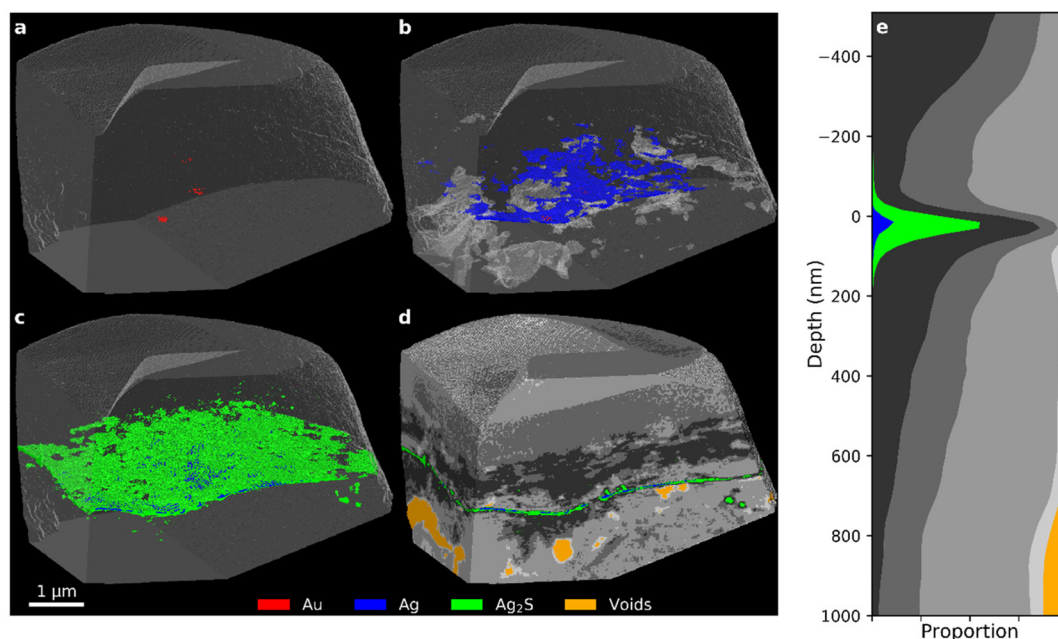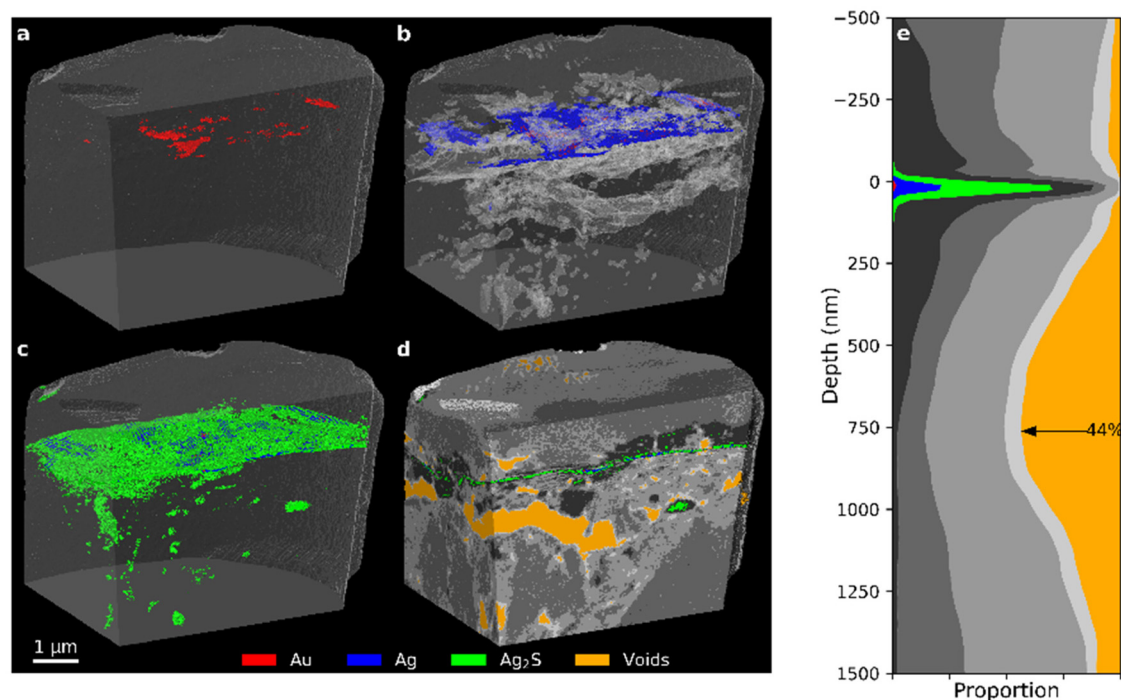

Fig. 10 (a–d) PXCT 3D images for different components (see Fig. 7 for segmentation details) inside the Sedrun *Nicolaus* sample. (e) Stack plot of the depth profile of the sample, aligned to the metal layer.

porous (31%) or is mixing with lower delta materials from the varnish. Our SEM-EDX observations indicate that each of these possibilities typically occur in different sites of each sample.

SEM-EDX observations on different sites of this sample show that S is spread quite evenly throughout the entire varnish layer and so the peak at delta value 9×10^{-6} could perhaps

Fig. 11 (a–d) PXCT 3D images for different components (see Fig. 7 for segmentation details) inside the Sedrun *Bishop* sample. (e) Stack plot of the depth profile of the sample, aligned to the upper surface of the metal layer.
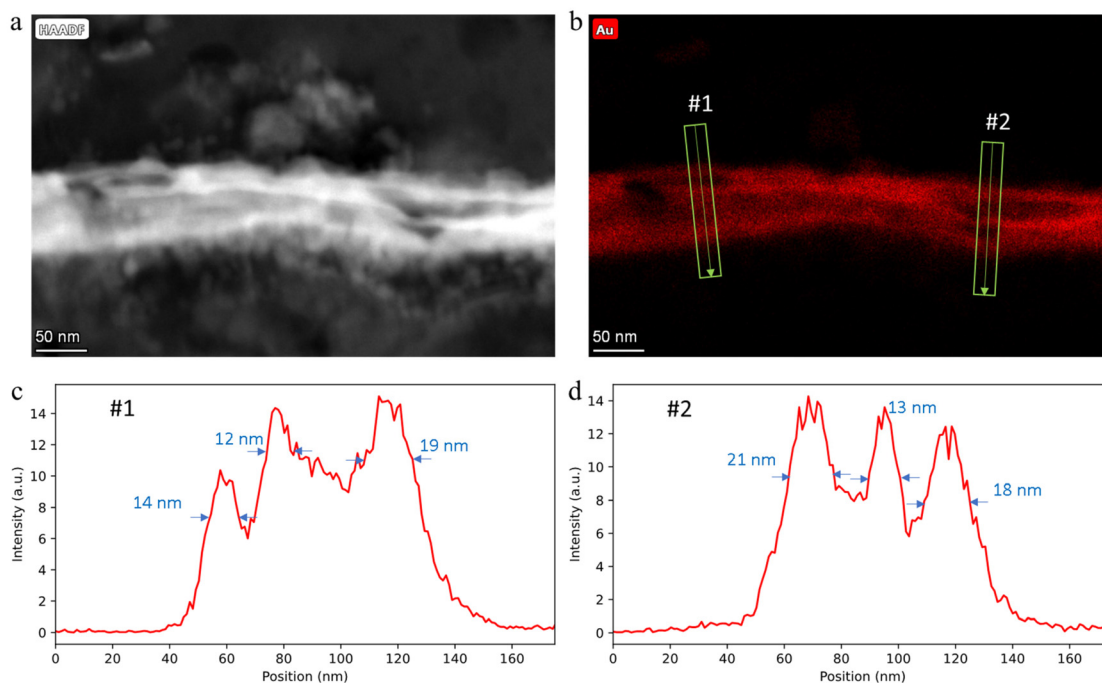
Fig. 12 STEM-EDX analysis of a sample taken in an adjacent region to the *Bishop* sample: (a) high-angle annular dark-field (HAADF) image and (b) EDX Au map of a Zwischgold leaf cross-section; (c and d) EDX line profile across the leaf along the green arrows in (b).

also be described as corresponding to a mixture of Ag_2S and organic varnish.

The *Nicolaus* sample taken from the centre of a corroded Zwischgold patch, Fig. 10, shows an extremely thin layer of high-δ voxels segmented into the Ag_2S, Ag and Au segments. This is also reflected in the histogram presented in Fig. 7, where the histogram drops rapidly above a δ value of about 17 $\times 10^{-6}$ due to the very low proportion of high δ voxels. This thin layer is consistent with a single Zwischgold Au-layer matching the two Zwischgold Au-layers that overlay the gold leaf in the *Nicolaus Border* sample. However, complementary SEM-EDX measurements on a sample cross-section that was taken in an adjacent region of the *Nicolaus* sample, show that the Zwischgold leaf contains both single and double Au layers (Fig. S11a and b in the ESI†), and their average layer thickness of 29 ± 10 nm (Fig. S11c†) is consistent with the PXCT data. Previous SEM-EDX measurements of the Ag : Au elemental ratio provide an estimated original total leaf thickness of 225 ± 78 nm.[38]

Unlike the *35-year* and *Mary* samples, both of the *Nicolaus* samples display only a few, poorly connected pores in the varnish and bole layers. Further, these pores do not show significant concentration adjacent to the Zwischgold leaf in these two *Nicolaus* samples, demonstrating that the voids and delamination effects observed in other samples are not simply due to the sample preparation methods.

The PXCT data of the *Bishop* sample presented in Fig. 11 shows another highly corroded Zwischgold leaf that appears similar to the *Nicolaus* sample and has a thickness similar to the measurement resolution of 39 nm (see Table 1). Close inspection of the gold layer in a FIB cross-section of a *Bishop* sample by STEM reveals a triple-layer structure, as shown in Fig. 12, with an average thickness of about 16 nm for each gold layer. This fine structure is below the resolution of the PXCT measurements and suggests that the Zwischgold leaf applied to the Sedrun *St. Bishop* belongs to a rarely-observed class of multi-layered Zwischgold leaves.[39] It is worth noting that the green segment representing corrosion products observed in Fig. 11 does not only reside above the original metal leaf position but is also distributed throughout the substrate, in the form of small aggregates. These aggregates distributed throughout the substrate could also be relatively large grains of iron oxide mixed with the bole substrate, since Fe_2O_3 has a δ value of 13.5×10^{-6}. A few large-sized voids and lots of smaller pores are present around the metal leaf and throughout the substrate of the *Bishop* sample, though with less delamination of the leaf than was observed in the *35-year* and *Mary* sample.

4 Conclusions

These pioneer PXCT measurements of both modern and medieval examples of Zwischgold have demonstrated the ability to reveal many features of thin, multi-layered metal leaves and their surroundings with a resolution better than 40 nm in

samples of more than 5 microns in size. The 3D images provide quantitative measures of the layer composition and thickness, as well as larger scale features, such as a fold in the metal leaf that has been flattened by burnishing in the case of the *35-year* sample. Importantly, the imaged structures can reside in regions away from the cutting face of the sampled material and fragile, porous structures can be observed with minimal alteration. This is important because strongly heterogenous samples like those examined in this work should be expected to display many cutting-face artefacts that would strongly limit the use of direct-sectioning tomography methods. For example, FIB/SEM tomography, which uses a focused ion beam to successively slice the sample and a scanning electron microscope to image each cross-section with nanoscale resolution, would be limited by curtaining artefacts where variations in sample hardness cause the cutting face to be significantly non-flat.[55] (An example SEM image of a FIB cross-section of the *Nicolaus border* sample that displays significant curtaining is shown in Fig. S17 of the ESI†).

The *Mary* sample, taken from the central figure of the Leiggern Altar is quite similar in thickness and structure to the modern Zwischgold, albeit with more lateral variation in the thickness of the gold layer. The Sedrun *Nicolaus* and *Bishop* samples, in contrast, are much thinner and are composed of multiple layers. Further study is required to determine if the Sedrun sculptures are of novel construction, or if ultra-thin, multi-layered Zwischgold leaves are actually more common than is currently understood. The thickness of the metal layers observed by PXCT was reasonably precise in cases where the measurement resolution was well below the layer thickness. However, one of the practical limits to the measurement resolution is the mechanical stability of the sample while measuring the set of projections, which was found to be unpredictable for historical samples. Complementary electron microscopy measurements proved invaluable for observing the fine, ultra-thin details of the historical Zwischgold leaves. Together, these observations provide insight into the relative value of higher resolution *versus* higher dimensional imaging techniques that can guide future studies.

The 3D imaging of PXCT also allowed us to assess the degree of adhesion (or connectedness) between the Zwischgold leaves and their bole substrates and varnish overlayers. Each of the samples that included a substrate displayed a series of voids within the substrate materials that were often concentrated near the leaf interface in a way that could be described as a partial delamination of the metal leaf. The *35-year* and the *Mary* samples displayed 84.7% and 53.9% delamination area (respectively) at the leaf-substrate interface, while the *Bishop* sample presented a 45.5% fracture surface about 750 nm below the metal leaf. The delamination patterns appear more consistent with expansion-contraction tensions, rather than being connected to corrosion mechanisms. A concentration of voids near the leaf-varnish interface was also observed in the *Mary*, *Nicolaus Border* and *Bishop* samples, covering 11.2%, 5.3% and 5.5% of the respective interfacial area. The quantitative nature of the PXCT data further allowed esti-

mation of the porosity of the corrosion products (*e.g.* 15% porous silver sulphide observed in the *Mary* sample) and even of the metallic silver (due to the Kirkendall effect).

This work has demonstrated PXCT as a powerful tool for quantitative three-dimensional characterisation of very heterogeneous samples. While the resolution of our measurements was not sufficient to fully resolve the very fine details of the *Nicolaus* and *Bishop* Zwischgold foils, there are a number of ways to improve future PXCT measurements. Firstly, cryo-preservation of the sample will help stop the sample from moving or changing shape during the measurement (this can happen due to radiation damage). Similarly, a more coherent X-ray source (from a diffraction limited synchrotron[56]) will improve the dose-efficiency of the PXCT measurements so that less radiation damage should occur. Secondly, improvements in the measurement rate due to improvements in detector hardware and photon flux of the X-ray beam can increase the rate of measurements so that further projections can be measured in the same amount of time. Finally, the reconstruction codes for analysing ptychographic and computed tomography datasets are undergoing rapid development that make them more tolerant of non-idealities in the raw data so that imaging artefacts can be minimised.

5 Methods

Applied Zwischgold samples were cut by focused ion-beam (FIB) into cylinders with a diameter of 5–10 μm; below the metal leaf part, an approximately 10 μm thick section of bole was retained as an isolation layer between the metal leaf and the sample holder. 10 × 10 μm squares of free-standing Zwishgold leaf were cut by FIB for the *Recent* and *10-year* samples. Transfer of the samples onto OMNY pin sample holders[57] were performed *via* FIB and an *in situ* micromanipulator. After removal of the cylinder, cross-sections of the remaining sample were trimmed by FIB and measured *in situ* by STEM or SEM, and EDX. TEM sample preparation and STEM-EDX measurements were performed at the University of Siegen (Siegen, Germany). The TEM cross-section lamellas were prepared with a Thermo Fischer FEI Helios 600 by applying a standard lift-out with final polishing at 2 kV. A Thermo Fischer FEI Talos F200X microscope, equipped with a SuperX-detector, operating at 200 kV was used for STEM-EDX analysis.

PXCT experiments[35,58] were carried out at the cSAXS beamline (X12SA) at the Swiss Light Source, Paul Scherrer Institut (PSI), Switzerland. A general description of the PXCT measurements is given as follows. A double crystal Si(111) monochromator was used to provide a monochromatic radiation of 8.7 keV generated by an in-vacuum undulator. The beam was focused by a Fresnel zone plate (FZP) with a diameter of 120 μm, outermost zone width of 60 nm (ref. 59) resulting in a focal distance of 51 mm. The FZP was fabricated in the Laboratory for Micro and Nanotechnology, Paul Scherrer Institut, Switzerland. The sample was placed 1 mm downstream of the focus to give an illumination of approximately

2.5 μm in diameter. The ptychography scans followed a Fermat spiral pattern[60] with an average step size of 0.6 μm over a field of view (FOV) of up to 15 μm horizontally by 6 μm vertically. Diffraction patterns were collected 7.4 m downstream of the sample using a Pilatus 2M detector[61] with an exposure time of 0.1 s. Projections were measured at uniform intervals of sample rotation from 0° to 180°, with about 4×10^7 incident photons per square micron, per projection. The ptychographic reconstruction of the 2D projections from sets of 400 by 400 pixel diffraction patterns was performed using the difference map[28] and maximum likelihood[62,63] methods to give an image pixel size of 15 nm (except for the *Recent* and *10-year* samples with voxel sizes of 12 and 20 nm respectively). Subsequently, projections were aligned[64,65] to give 3D tomograms based on modified filtered back projection.[64] The tomogram half-pitch resolution was estimated by Fourier shell correlation half bit criteria[66] to be between 18 and 35 nm, depending on the sample. Table 1 provides the specific PXCT imaging parameters for each sample. The β and δ parts of the reconstructed data were observed to provide the same information, but with lower noise in the δ values, and so the β part was discarded.

Data obtained from PXCT experiments was processed in Avizo 9.5 for quantitative analysis and 3D visualization. An important step to reach this goal is the segmentation of materials of interest, *i.e.* dividing the data array into materials zones based on their δ-value (which correlates closely with electron density when the X-ray energy is not close to an elemental resonance[67]). The most interesting materials in Zwischgold samples are Au and Ag, the main Ag corrosion products such as Ag_2S and $AgCl$, and materials expected to be present in the varnish coating and bole substrates. Quartz (SiO_2), kaolinite ($Al_2Si_2O_5(OH)_4$), Na_2SiO_3, $Mg_3Si_4O_{10}(OH)_2$) and calcite ($CaCO_3$) are main bole materials.[68] The earth pigments red ochre (main component hematite Fe_2O_3) and yellow ochre (main component goethite $FeO(OH)$) were commonly mixed with bole materials to make red and yellow boles. Other materials that are expected to be observed include amorphous carbon and aluminium as protective and conductive coatings, as well as gallium which was used as the FIB ion source. The δ and β values for 8.7 keV photons interacting with materials of interest in Zwischgold samples were calculated using the atomic scattering factors from Henke *et al.*[67] and presented in Table S1 in the ESI.†

Author contributions

B. W., Q. W., K. S., and R. H. F conceptualised the study. Q. W. and E. M. prepared the PXCT samples and J. M. prepared the TEM samples. B. W., Q. W., E. H. R. T, M. H., and M. G.-S. performed the PXCT measurements. M. O., E. H. R. T., and M. G.-S. performed the PXCT reconstructions. B. W. and Q. W. analysed the 3D data sets. Q. W. performed the SEM measurements, J. M. and B. B. performed the TEM measurements and A. S. performed the XPS measurements. B. W. and Q. W. wrote the original draft with contributions, editing and review from all authors.

Conflicts of interest

There are no conflicts of interest to declare.

Acknowledgements

References

1 B. Reudenbach, Gold is Schlamm, in *Material in Kunst und Alltag*, Akademrie Verlag, Berlin, 2002, pp. 1–12.

2 S. Kubersky-Piredda, The Market for Painters' Materials in Renaissance Florence, in *Trade in Artists' Materials: Market and Commerce in Europe to 1700*, Archetype Publications, London, 2010, pp. 223–243.

3 S. Nash, 'Pour couleurs et autres choses prise de lui...': The Supply, Acquisition, Cost and Employment of Painters Materials at the Burgundian Court, c.1375–1419, in *Trade in Artists Materials: Markets and Commerce in Europe to 1700*, Archetype Publications, London, 2010, pp. 987–182.

4 J. M. Nadolny, *The techniques and use of gilded relief decoration by northern European painters, C. 1200–1500*, Doctor Thesis, Courtauld Institute of Art, London, 2000, (Chapter 8).

5 M. Eveno and E. Martin, *Les feuilles mixtes or-argent en peinture de chevalet. ICOM Committee for Conservation. Painting II: Scientific study of paintings*, James & James, London, 1996, pp. 355–359.

6 M. Eveno, E. Ravaud, T. Calligaro, L. Pichon and E. Laval, The Louvre crucifix by Gioto: Unveiling the original decoration by 2D-XRF, X-ray radiography, Emissiography and SEM-EDX analysis, *Heritage Sci.*, 2014, **2**, 17, DOI: 10.1186/s40494-014-0017-y.

7 I. Osticioli, L. Capozzoli, B. Salvadori, M. Banchelli, A. Lavacchi, P. Matteini, S. Siano and L. Gallo, The oro di metà Gilding in the Fifteenth-Century: A Multi-Analytical Investigation, *Heritage*, 2019, **2**(2), 1166–1175, DOI: 10.3390/heritage2020076.

8 R. E. Straub, Tafel- und Tüchleinmalerei des Mittelalters, in *Reclams Handbuch der künstlerischen Techniken. Bd. 1*, Philipp Reclam jun., Stuttgart, 1984, pp. 131–259.

9 C. Zindel, *Güldene Kunst-Pforte: Quellen zur Kunsttechnologie*, Westermann Druck, Zwickau, 2010, p. 679.

10 E. Skaug, 'Delt Gull' – 'Laminatgull'? Problemer i medelalderens förgyllningstekkniker, in *Preprints nordisk Konservatorförbunds Kongress 9, 25–29 mai*, 1981.

11 J. Nadolny, Some Observations on Northern European Metalbeaters and Metal Leaf in the Late Middle Ages, in *The Materials, Technology and Arts of Conservations*, Conservation Centre of the Institute of Fine Arts, New York University, 1999.

12 J. S. Halle, *Werkstäte der heutigen Künste oder die neue Kunsthistorie, Band. 1*, Brandenburg, 1761, pp. 174–175.

13 V. Passeri, Gold coins and gold leaf in early Italian paintings, in *The matter of art: materials, practices, cultural logics, c. 1250–1750*, Manchester University Press, Manchester, 2015, p. 97.

14 J. C. M. Hwang, J. D. Pan and R. W. Balluffi, Measurement of grain-boundary diffusion at low temperature by the surface accumulation method. II. Results for gold-silver system, *J. Appl. Phys.*, 1979, **50**, 1349, DOI: 10.1063/1.326115.

15 Q. Wu, K. Soppa, N. Scherrer, B. Watts, T. Yokosawa, L. Bernard, T. Araki, M. Döbeli, M. Meyer, E. Spiecker and R. H. Fink, Investigation of the foil structure and corrosion mechanisms of modern Zwischgold using advanced analysis techniques, *J. Cultural Heritage*, 2018, **31**, 122–132, DOI: 10.1016/j.culher.2017.12.005.

16 H. Huth, in *Künstler und Werkstatt der Spätgotik*, Wissenschaftliche Buchgesellschaft, Darmstadt, 3rd edn, 1977, pp. 97–98.

17 T. Brachert, Die Techniken der polychromierten Holzskulptur, *Maltechnik Restauro*, 1972, **78**, 153–204.

18 R. Kühnen, *Der Ortenberger Altar aus dem Hessischen Landesmuseum Darmstadt: Untersuchungen und Anmerkungen zu technologischen Besonderheiten*, Akademie der Bildenden Künste Stuttgart, Diplomarbeit, 1997, pp. 31, 69–77.

19 F. Preusser, Die naturwissenschaftliche Untersuchung der Grünewaldtafelnaus Lindenhardt und ihre Ergebnisse, in *Die Lindenhardter Tafelbilder von Matthias Grünewald*, Bayerisches Landesamt für Denkmalpfleg, München, 1978, p. 20.

20 P. Tångeberg, *Mittelalterliche Holzskulpturen und Altarschreine in Schweden: Studien zu Form, Material und*

Technik. Kungl, Vitterhets Historie och Antikvitets Akademien, Stockholm, 1986, pp. 223–227.

21 F. Buchenrieder, *Gefasste Bildwerke: Untersuchung und Beschreibung von Skulpturenfassungen mit Beispielen aus der praktischen Arbeit der Restaurierungswerkstätten des Bayerischen Landesamtes für Denkmalpflege 1958-1986*, Bayerisches Landesamt für Denkmalpflege, München, 1990, pp. 73–74.

22 R. E. Straub, E.-L. Richter, H. Härlin and W. Brandt, Der Magdalenenaltar des Lucas Moser, eine technologische Studie, in *Beiträge zur Untersuchung und Konservierung mittelalterlicher Kunstwerke*, Deutscher Kunstverlag, München, 1974, p. 41.

23 K. Wittenburg, *Der Traminer Altar im Bayerischen Nationalmuseum, München: Studien zu dem Hans Klocker zugeschriebenen Retabel. Diplomarbeit*, Technische Universität München, 2004, pp. 32, 39, 47, 48, 53, 59, 84 &108.

24 T. Bullinger, *Der Leiggerner Altar im Schweizer Landesmuseum: Eine kunstgeschichtliche und technologische Monographie*, Dissertation, Urbach, 1974, vol. **226**, pp. 178–180.

25 Q. Wu, M. Wörle, V. Hubert, E. Müller, M. Haudenschild, P. Wyer, N. Scherrer and K. Soppa, The identification of Zwischgold and other metal foils on historical sculptures by handheld XRF spectrometry, *Z. Kunsttechnol. Konserv*, 2018, **32**(1), 55–68.

26 Q. Wu, T. Lombardo, V. Hubert, E. Hildbrand, P. Wyer, F. Nolting and D. Ganz, New insights into Zwischgold application from a multi-analytical survey of late medieval polychrome sculptures at the Swiss National Museum, *Microchem. J.*, 2020, **156**, 104810, DOI: **10.1016/j.microc.2020.104810**.

27 A. Roy, Methods and materials of Northern European painting in the National Gallery, 1400-1500, *Natl. Gallery Tech. Bull.*, 1997, **18**, 6–55 **https://www.nationalgallery.org.uk/technical-bulletin/methods_and_materials1997**.

28 P. Thibault, M. Dierolf, A. Menzel, O. Bunk, C. David and F. Pfeiffer, High-resolution scanning x-ray diffraction microscopy, *Science*, 2008, **321**, 379–382, DOI: **10.1126/science.1158573**.

29 M. Dierolf, A. Menzel, P. Thibault, P. Schneider, C. M. Kewish, R. Wepf, O. Bunk and F. Pfeiffer, Ptychographic X-ray computed tomography at the nanoscale, *Nature*, 2010, **467**, 436–439, DOI: **10.1038/nature09419**.

30 A. Diaz, P. Trtik, M. Guizar-Sicairos, A. Menzel, P. Thibault and O. Bunk, Quantitative x-ray phase nanotomography, *Phys. Rev. B: Condens. Matter Mater. Phys.*, 2012, **85**, 020104, DOI: **10.1103/PhysRevB.85.020104**.

31 M. Guizar-Sicairos and P. Thibault, Ptychography: A solution to the phase problem, *Phys. Today*, 2021, **74**, 42–48.

32 H. M. L. Faulkner and J. M. Rodenburg, Movable aperture lensless transmission microscopy: a novel phase retrieval algorithm, *Phys. Rev. Lett.*, 2004, **93**, 023903, DOI: **10.1103/PhysRevLett.93.023903**.

33 J. Rodenburg, A. Hurst, A. Cullis, B. Dobson, F. Pfeiffer, O. Bunk, C. David, K. Jefimovs and I. Johnson, Hard-X-ray lensless imaging of extended objects, *Phys. Rev. Lett.*, 2007, **98**, 034801, DOI: **10.1103/PhysRevLett.98.034801**.

34 Y. Liu, J. Nelson, C. Holzner, J. C. Andrews and P. Pianetta, Recent advances in synchrotron-based hard x-ray phase contrast imaging, *J. Phys. D*, 2013, **46**, 494001.

35 M. Holler, A. Diaz, M. Guizar-Sicairos, P. Karvinen, E. Färm, E. Härkönen, M. Ritala, A. Menzel, J. Raabe and O. Bunk, X-ray ptychographic computed tomography at 16 nm isotropic 3D resolution, *Sci. Rep.*, 2014, **4**, 3857, DOI: **10.1038/srep03857**.

36 M. Holler, M. Guizar-Sicairos, E. H. R. Tsai, R. Dinapoli, E. Müller, O. Bunk, J. Raabe and G. Aeppli, High-resolution non-destructive three-dimensional imaging of integrated circuits, *Nature*, 2017, **543**, 402–406, DOI: **10.1038/nature21698**.

37 H. Yuan, H. Yuan, T. Casagrande, D. Shapiro, Y.-S. Yu, B. Enders, J. R. I. Lee, A. van Buuren, M. M. Biener, S. A. Gammon, T. F. Baumann and A. P. Hitchcock, 4D Imaging of ZnO-Coated Nanoporous Al2O3 Aerogels by Chemically Sensitive Ptychographic Tomography: Implications for Designer Catalysts, *ACS Appl. Nano Mater.*, 2021, **4**, 621–632, DOI: **10.1021/acsanm.0c02924**.

38 Q. Wu, B. Watts, M. Döbeli, J. Müller, B. Butz, T. Lombardo, K. Schmidt-Ott, R. Fink, F. Nolting and D. Ganz, Medieval nanotechnology: Thickness determination of Zwischgold samples, *J. Cultural Heritage*, 2021, **49**, 211–221, DOI: **10.1016/j.culher.2021.01.010**.

39 Q. Wu, T. Lombardo, V. Hubert, E. Hildbrand, P. Wyer, K. Schmidt-Ott, R. Fink, B. Watts and F. Nolting, *Observation and analysis of Zwischgold in late medieval sculptures. ICOM-CC 19th Triennial Conference Preprints*, ed. J. Bridgland, Paris, International Council of Museums, Beijing, 17–21 May 2021.

40 L. Dussubieux and L. van Zelst, LA-ICP-MS analysis of platinum group elements and other elements of interest in ancient gold, *Appl. Phys. A*, 2004, **79**, 353–356, DOI: **10.1007/s00339-004-2532-2**.

41 M. F. Guerra, An overview on the ancient goldsmith's skill and the circulation of gold in the past: the role of X-ray based techniques, *X-ray Spectrom.*, 2008, **37**, 317–327, DOI: **10.1002/XRS.1013**.

42 D. Flühler-Kreis and P. Wyer, *Maria mit Kind, drei Könige mit Stifterfigur, Martyrium des heiligen Romanus. Baldachinretabel*, in *Die Holzskulpturen des Mitterlalters II - Katalog der Sammlung des Schweizerischen Landesmuseum Zürich II: Altarretabel und retabelfiguren*, Schweizerisches Landesmuseum, Zürich, 2007, pp. 24–29.

43 T. Brachert and F. Kobler, *Fassung von Bildwerken. In Gefasste Bildwerke: Untersuchung und Beschreibung von Skulpturenfassungen mit Beispielen aus der praktischen Arbeit der Restaurierungswerkstätten des Bayerischen Landesamtes für Denkmalpflege 1958-1986*, Bayerisches Landesamt für Denkmalpflege, München, 1990, pp. 322, 329–330.

44 D. Hradil, J. Hradilová, P. Bezdicka and C. Serendan, Late Gothic/early Renaissance gilding technology and the traditional poliment material 'Armenian bole': Truly red clay, or rather bauxite?, *Appl. Clay Sci.*, 2017, **135**, 271–281, DOI: **10.1016/j.clay.2016.10.004**.

45 R. E. Straub, Tafel- und Tüchleinmalerei des Mittelalters, in *Reclams Handbuch der künstlerischen Techniken. Bd. 1*, Philipp Reclam jun., Stuttgart, 1984, pp. 213–214.

46 S. Zumbühl and C. Zindel, *Historical siccatives for oil paint and varnishes - The use of lead oxide, alum, white vitriol, pumice, bone ash and venetian glass as driers: Historical written sources - production and raw material quality - technological significance*, HDW Publications Bern, 2022, pp. 26.

47 A. Bartl, *Personal communication between Anna Bartl and Qing Wu via email in April*, 2017.

48 A. Bukaluk, Analysis of diffusion mechanisms in thin polycrystalline Au-Ag films using Auger electron spectroscopy, *Surf. Interface Anal.*, 1983, **5**, 20–27, DOI: **10.1002/sia.740050106**.

49 R. G. Kirsch, J. M. Poate and M. Eibschutz, Interdiffusion mechanisms in Ag-Au thin-film couples, *Appl. Phys. Lett.*, 1976, **29**, 772, DOI: **10.1063/1.88944**.

50 T. E. Jones, S. Piccinin and C. Stampfl, Relativity and the nobility of gold, *Mater. Chem. Phys.*, 2013, **141**, 14–17, DOI: **10.1016/j.matchemphys.2013.04.049**.

51 J. M. Poate, Diffusion and Reactions in Gold Films: A Review of Fundamental Aspects, *Gold Bull.*, 1981, **14**, 2–11.

52 F. Seitz, On the porosity observed in the Kirkendall effect, *Acta Metall.*, 1953, **1**, 355–369, DOI: **10.1016/0001-6160(53)90112-6**.

53 T. Ishitana and H. Kaga, Calculation of local temperature rise in focused-ion-beam sample preparation, *J. Electron Microsc.*, 1995, **44**, 331–336, DOI: **10.1093/oxfordjournals.jmicro.a051185**.

54 K. Kitagawa, On the development of the (001) texture of gold leaf by hammering, *J. Mater. Sci.*, 1988, **23**, 2810–2814.

55 F. Lutter, P. Stahlhut, K. Dremel, S. Zabler, J. Fell, H.-G. Herrmann and R. Hanke, *Combining X-ray Nano Tomography with focused ion beam serial section imaging— Application of correlative tomography to integrated circuits Nuclear Instruments and Methods in Physics Research Section B: Beam Interactions with Materials and Atoms*, 2021, vol. 500–501, pp. 10–17. DOI: **10.1016/j.nimb.2021.05.006**.

56 A. Streun, T. Garvey, L. Rivkin, V. Schlott, T. Schmidt, P. Willmott and A. Wrulich, SLS-2 – the upgrade of the Swiss Light Source, *J. Synchrotron Rad.*, 2018, **25**, 631–641, DOI: **10.1107/S1600577518002722**.

57 M. Holler, J. Raabe, R. Wepf, S. H. Shahmoradian, A. Diaz, B. Sarafimov, T. Lachat, H. Walther and M. Vitins, OMNY PIN-A versatile sample holder for tomographic measurements at room and cryogenic temperatures, *Rev. Sci. Instrum.*, 2017, **88**, 113701, DOI: **10.1063/1.4996092**.

58 M. Holler, J. Raabe, A. Diaz, M. Guizar-Sicairos, C. Quitmann, A. Menzel and O. Bunk, An instrument for 3d x-ray nano-imaging, *Rev. Sci. Instrum.*, 2012, **83**, 073703, DOI: **10.1063/1.4737624**.

59 S. Gorelick, J. Vila-Comamala, V. A. Guzenko, R. Barrett, M. Salomé and C. David, High-efficiency Fresnel zone plates for hard X-rays by 100 keVe-beam lithography and electroplating, *J. Synchrotron Radiat.*, 2011, **18**, 442–446, DOI: **10.1107/s0909049511002366**.

60 X. Huang, H. Yan, R. Harder, Y. Hwu, I. K. Robinson and Y. S. Chu, Optimization of overlap uniformness for ptychography, *Opt. Express*, 2014, **22**, 12634–12644, DOI: **10.1364/OE.22.012634**.

61 B. Henrich, A. Bergamaschi, C. Broennimann, R. Dinapoli, E. F. Eikenberry, I. Johnson, M. Kobas, P. Kraft, A. Mozzanica and B. Schmitt, Pilatus: A single photon counting pixel detector for x-ray applications, *Nucl. Instrum. Methods Phys. Res., Sect. A*, 2009, **607**, 247–249, DOI: **10.1016/j.nima.2009.03.200**.

62 M. Guizar-Sicairos and J. R. Fienup, Phase retrieval with transverse translation diversity: a nonlinear optimization approach, *Opt. Express*, 2008, **16**, 7264–7278, DOI: **10.1364/OE.16.007264**.

63 P. Thibault and M. Guizar-Sicairos, Maximum-likelihood refinement for coherent diffractive imaging, *New J. Phys.*, 2012, **14**, 063004, DOI: **10.1088/1367-2630/14/6/063004**.

64 M. Guizar-Sicairos, A. Diaz, M. Holler, M. S. Lucas, A. Menzel, R. A. Wepf and O. Bunk, Phase tomography from x-ray coherent diffractive imaging projections, *Opt. Express*, 2011, **19**, 21345–21357, DOI: **10.1364/OE.19.021345**.

65 M. Guizar-Sicairos, J. J. Boon, K. Mader, A. Diaz, A. Menzel and O. Bunk, Quantitative interior x-ray nanotomography by a hybrid imaging technique, *Optica*, 2015, **2**, 259–266, DOI: **10.1364/OPTICA.2.000259**.

66 M. van Heel and M. Schatz, Fourier shell correlation threshold criteria, *J. Struct. Biol.*, 2005, **151**, 250–262, DOI: **10.1016/j.jsb.2005.05.009**.

67 B. L. Henke, E. M. Gullikson and J. C. Davis, ., X-ray interactions: photoabsorption, scattering, transmission, and reflection at E = 50-30000 eV, Z = 1-92, *At. Data Nucl. Data Tables*, 1993, **54**(2), 181–342, DOI: **10.1006/adnd.1993.1013**.

68 N. Salvado, S. Buti, A. Labrador, G. Cinque, H. Emerich and T. Pradell, SR-XRD and, SR-FTIR study of the alteration of silver foils in medieval paintings, *Anal. Bioanal. Chem.*, 2011, **399**, 3041–3052, DOI: **10.1007/s00216-010-4365-5**.